Supporting Information

Radical-Driven Nano-Crystalline IrO_2: Resolving the Activity-Stability Trade-Off in Acidic OER

Renxing Huang[a, b #], Zeping Zhang[b #], Chengcheng Sang[b, c], Weitao Gao[d], Yiming Bai[b], Yinghe Huang[a, b], Yuxing Shi[a], Yonghuan Li[a], Lianguo Sun[b], Cheng Wang[b*], Jun Gu[a*] ，Tao Yu[a*]

[a] School of Physics, Nanjing University, Nanjing, 210093, China;

[b] Division of New Energy Material and Chemical Engineering, INET, Tsinghua University, Beijing, 100084, China;

[c] College of Mechanical and Vehicle Engineering, Hunan University, Changsha 410082, China;

[d] College of Mechanical and Electrical Engineering, Central South University, Changsha, 410083, China

*Corresponding authors. Email: wangcheng@tsinghua.edu.cn (C. W); junguca@nju.edu.cn (J. G); yutao@nju.edu.cn (T.Y)

Chemicals

Hexachloroiridic acid ($H_2IrCl_6 \cdot xH_2O$), hexachloroplatinic(IV) acid ($H_2PtCl_6 \cdot xH_2O$), ruthenium(III) chloride ($RuCl_3$), and potassium tetrachloropalladate ($K_2PdCl_4 \cdot xH_2O$) were purchased from Changzhou Yiding Metal Co., Ltd. Hydrogen peroxide (30% H_2O_2), Sodium bisulfite ($NaHSO_3$), Sodium carbonate (Na_2CO_3), Sodium hydroxide (NaOH) and perchloric acid ($HClO_4$) were purchased from Sinopharm Chemical Reagent Co., Ltd. Nafion® perfluorinated resin solution (5 wt%) from Sigma-Aldrich. Commercial 40% Pt/C was produced by TsingHydrogen Technology Co., Ltd. The commercial Iridium oxide (IrO_2) catalyst was purchased from Heraeus (China). The batch number is 9016862119. All the chemicals and reagents were used without further purification.

Characterization

Aberration-corrected high-angle annular dark-field scanning transmission electron microscopy (HAADF-STEM) was conducted using a Thermo Scientific Spectra 200 microscope with a cold-field emission gun operated at 200 kV. Prior to imaging, the catalyst powders were ultrasonically dispersed in ethanol for 30 min, and a drop of the suspension was deposited onto a lacey carbon-coated Cu grid and dried under ambient conditions.

Conventional TEM and high-resolution TEM (HRTEM) were performed on an FEI Talos F200X instrument operated at 200 kV. Energy-dispersive X-ray spectroscopy (EDS) was conducted using the same microscope equipped with a Super-X EDS system comprising four windowless silicon drift detectors (SDDs) for high-efficiency elemental mapping. Samples were prepared by dispersing the powdered material in ethanol, drop-casting onto carbon-coated Cu grids, and drying in air.

UV-vis absorption spectra were acquired using a Mini-1200 spectrophotometer in the 300-700 nm range. Liquid samples were measured in quartz cuvettes with an optical path length of 1 cm. The reaction solution during the reaction process is directly tested after being diluted with ultrapure water.

X-ray diffraction (XRD) patterns were recorded on a Bruker D8 Advance diffractometer using Cu Kα radiation (λ = 1.5406 Å), scanned at 5° min^{-1} from 10° to 90° (2θ). Samples were gently ground in an agate mortar and evenly spread on a low-background silicon sample holder before measurement.

X-ray photoelectron spectroscopy (XPS) was carried out on a Thermo Scientific K-Alpha spectrometer with monochromatic Al Kα radiation (hν = 1486.8 eV). The powders were pressed onto conductive carbon tape and mounted on the sample stage; binding energies were calibrated using the C 1s peak at 284.8 eV.

Electron paramagnetic resonance (EPR) spectra were collected using a JEOL JES-FA200 spectrometer. The reaction solution during the reaction process were loaded into quartz EPR tubes and sealed prior to measurement.

Elemental analysis was conducted using inductively coupled plasma optical emission spectrometry (ICP-OES, PerkinElmer Optima 8300). For ICP analysis, during the durability test, 2 mL of the reaction solution was directly taken and diluted to 5 mL with ultrapure water, then directly tested.

X-ray absorption spectroscopy (XAS), including X-ray absorption near-edge structure (XANES) and extended X-ray absorption fine structure (EXAFS), was performed at the BL14W1 beamline of the Shanghai Synchrotron Radiation Facility (SSRF). The storage ring operated at 3.5 GeV with a typical current of 220-260 mA. A Si(111) double-crystal monochromator was used for energy selection. The incident (I_0) and transmitted (I_t) X-ray intensities were monitored using ionization chambers filled with N_2/He mixtures optimized for the Ir L_3-edge. Powder samples were thoroughly mixed with boron nitride (BN) and pressed into pellets (diameter 10 mm) to obtain an edge step of approximately $\Delta\mu x \approx 1$. All measurements were collected in transmission mode at room temperature. The energy scale was calibrated using an Ir foil reference simultaneously measured, with the Ir L_3-edge set to 11215 eV. Data reduction and EXAFS fitting were carried out using the Demeter package (Athena and Artemis). Background subtraction, normalization, and Fourier transforms were performed

following standard procedures, with k^3-weighting applied to EXAFS χ(k) functions.

Electrochemical measurements for a three-electrode system

The oxygen evolution reaction (OER) electrocatalytic performance was evaluated using a CHI 660E electrochemical workstation (CH Instruments, Inc.) in a standard three-electrode system. Catalyst ink was prepared by ultrasonically dispersing 4 mg catalyst powder in a mixed solvent containing 600 μL isopropanol, 400 μL ultrapure water, and 20 μL Nafion® solution (5 wt%) for 1 h. Subsequently, 6 μL of the well-dispersed ink was drop-cast onto a mirror-polished glassy carbon electrode (GCE, 4 mm diameter), followed by natural drying under ambient conditions.

Electrochemical measurements were conducted using a rotating disk electrode (RDE) at 1600 rpm in 0.1 M $HClO_4$ electrolyte. A platinum wire and an Ag/AgCl (saturated KCl) electrode were used as the counter and reference electrodes, respectively. A glassy carbon RDE (4 mm diameter) served as the working electrode. All potentials were converted to the reversible hydrogen electrode (RHE) scale. Linear sweep voltammetry (LSV) scans were performed from 1.2 to 1.7 V vs. RHE at a scan rate of 5 mV s^{-1} with 100% iR-compensated. All potentials and converted to the RHE scale according to the following equation:

$$E_{vs.RHE} = E_{vs.\mathrm{Ag/AgCl}} + 0.244\ V + 0.059\ pH \qquad (1)$$

where 0.244 V is the potential difference between the Ag/AgCl (saturated KCl) reference electrode and the RHE in 0.1 M $HClO_4$.

Electrochemical impedance spectroscopy (EIS) measurements were conducted at 1.5 V vs. RHE with the frequency range of 100 kHz to 0.01 Hz. Catalyst durability was assessed via chronopotentiometry (CP) at a constant current density of 10 mA cm^{-2} on a carbon paper electrode (geometric area: 1 cm^2).

The S-number, a stability descriptor defined as the ratio of evolved O_2 to dissolved metal ions, was calculated using:

$$S-number=\frac{n_{O_2}}{n_{Ir}(dissolved)} \quad (2)$$

Where $n_{O_2}$is the molar number of O_2 produced, assuming 100% Faradaic efficiency, and n_{Ir} is determined via ICP-MS.

The turnover frequency (TOF) at 1.53 V (vs. RHE) was calculated assuming the Faradaic efficiency of 100% according to Equation (3):

$$TOF=\frac{J\times A}{4\times F\times M} \quad (3)$$

Where J is the current density (mA cm^{-2}), A is the geometric area of the work electrode, F is the Faraday constant (96485 C mol^{-1}), m is the mole number of metal on the electrode, and 4 is the number of electrons involved in forming one O_2 molecule.

Electrochemical measurements in PEM electrolyser

Proton exchange membrane water electrolyzer (PEMWE) tests were performed to assess the practical applicability of the catalysts. Membrane electrode assemblies (MEAs) were fabricated by ultrasonic spray-coating catalyst inks onto both sides of a Nafion 115 membrane. IrO_2(Sub-2 nm) or commercial IrO_2 was used as the anode catalyst (0.3 mg cm^{-2}), and commercial Pt/C (40 wt%) as the cathode catalyst (0.1 mg cm^{-2}). Loadings were verified via X-ray fluorescence (XRF).

Catalyst inks were prepared by dispersing the catalyst in a water/isopropanol (2:8 v/v) solvent mixture containing Nafion ionomer (10 wt% for the anode, 35 wt% for the cathode). The inks were homogenized via probe sonication in an ice-water bath for 1 h.

The electrolyzer employed Pt-coated titanium felt as the anode porous transport layer (PTL) and carbon paper as the cathode gas diffusion layer, with an active area of 25 cm^2. PEM electrolyzer performance evaluation was carried out using deionized water as the reactant feed, and the cell temperature was maintained at 80 °C. Polarization curves of the PEM electrolyzer were collected in the voltage range of 1.4-2.1 V using Gamry Instrument. Long-term stability assessment was performed via

chronopotentiometry at a constant current density of 1.0 A cm^{-2}. The high-frequency resistance was measured in the frequency range of 100 kHz to 0.01 Hz at 1.50 V.

(1) Overpotential analysis

The cell voltage (E_{cell}) during PEMWE operation consists of four components:

$$E_{cell} = E^0_{rev} + \eta_{kin} + \eta_{ohm} + \eta_{mt} \quad (1)$$

Where E^0_{rev} is the reversible potential, η_{kin}, η_{Ω}, and η_{mt} are the kinetic, ohmic, and mass transport overpotentials, respectively.

The temperature-dependent standard reversible potential, E^0_{rev}, is determined as

$$E_{rev} = E^0_{rev} + \frac{RT}{2F}\ln\frac{a\,(H_2)\sqrt{a\,(O_2)}}{a(H_2O)} \quad (2)$$

R is the ideal gas constant, T is the temperature, and F is Faraday's constant. At 80 °C, $a(H_2O) = 1$ and partial pressures of H_2 and O_2 at saturation, this yields the actual cell thermodynamic voltage.

$$E^0_{rev} = 1.2291 - 0.0008456*(T-298.15) \quad (3)$$

Ohmic overpotential was determined according to Equation (4):

$$\eta_{ohm} = j \times HFR\ (V) \quad (4)$$

Where j is the current density (A cm^{-2}), HFR is the high-frequency resistance obtained via EIS.

The kinetic overpotential was derived from Tafel fitting of the iR-corrected polarization curves between 4-20 mA cm^{-2}:

$$\eta_{kin} = b \times \log\left(\frac{j}{j_0}\right)\ (V) \quad (5)$$

Where b is the Tafel slope and j_0 is the exchange current density.

Finally, the value of η_{trans} was obtained by Equation (6):

$\eta_{trans} = E_{ohmic\text{-}corrected} - E_{kin}$（V） (6)

(2) The Construction of E-pH Diagrams

To construct the E-pH diagram, the following thermodynamic equations were applied:

(1) Gibbs free energy change for a reaction:

$\Delta G^0(reaction) = \Sigma \Delta G^0(products) - \Sigma \Delta G^0(reactants)$

(2) Standard electrode potential from Gibbs free energy:

$E^0 = \Delta G^0/-96.49n$

(3) Nernst equation for pH-dependent redox potentials:

$E = E^0 - RT/nF \ln[(products) / (reactants)]$

Based on the description above, E-pH diagrams for the $IrO_2/Ir(OH)_6^{3-}$ redox pair were constructed based on thermodynamic data obtained from Lange's Handbook of Chemistry.

$\Delta G^0(IrO_2) = -64.0$ kJ mol^{-1}, $\Delta G^0(Ir(OH)_6^{3-}) = -920.5$ kJ mol^{-1}, $\Delta G^0(H_2O) = -237.2$ kJ mol^{-1}, $\Delta G^0(OH^-) = -157.3$ kJ mol^{-1}, $\Delta G^0(H^+) = 0$ kJ mol^{-1}

$IrO_2 + e + 2OH^- + 2H_2O \rightarrow Ir(OH)_6^{3-}$

$-64.0 \quad -157.3 \times 2 \quad -237.2 \times 2 \quad -920.5$

$\Delta G^0(reaction) = \Sigma \Delta G^0(products) - \Sigma \Delta G^0(reactants)$

$\Delta G^0(IrO_2/ Ir(OH)_6^{3-}) = -67.5$ kJ mol^{-1}

$\Delta E^0 = \Delta G^0/ -96.49n = 0.70$ V

$E = E^0 - RT/nF \log ([products] / [reactants])$

$= 0.70 - 0.0591/n \log([Ir(OH)_6^{3-}]/ [OH^-]^2)$

$= 0.70 - 0.0591/1 \{\log([0.004]/ [OH^-]^2)\}$

$= -0.811 + 0.118$ pH

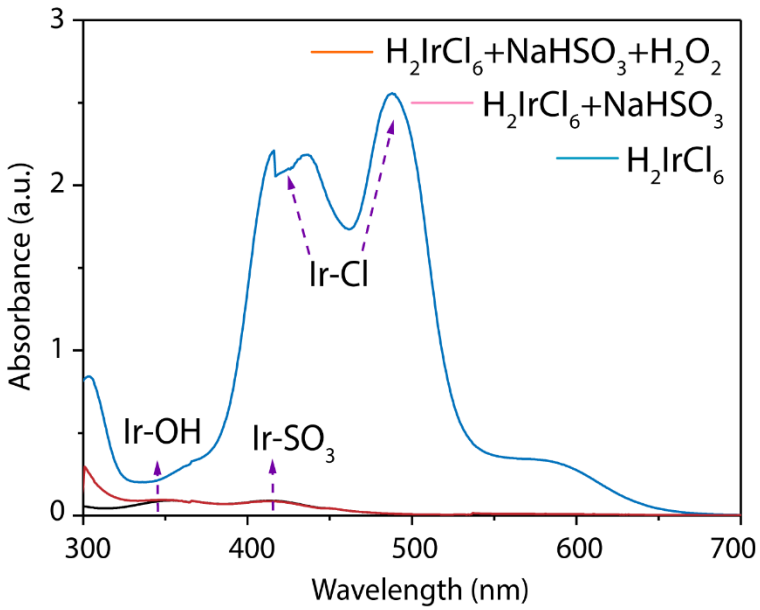

Fig. S1. UV-vis spectra of different chemicals in solution at room temperature.

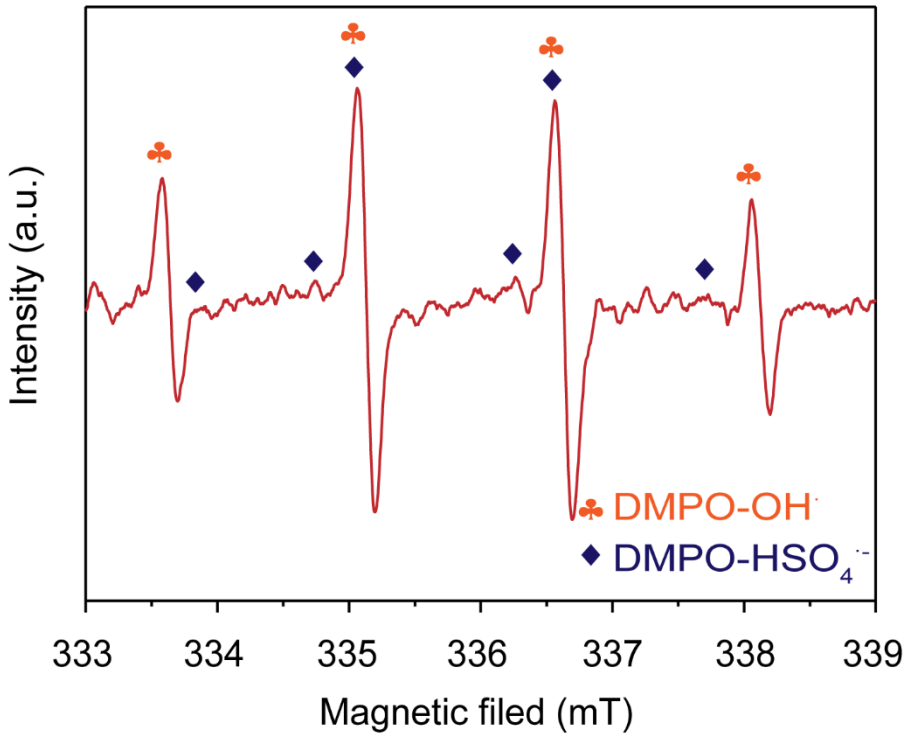

Fig. S2 EPR spectra confirming the presence of •OH radicals in $NaHSO_3$-H_2O_2 system via DMPO spin-trapping.

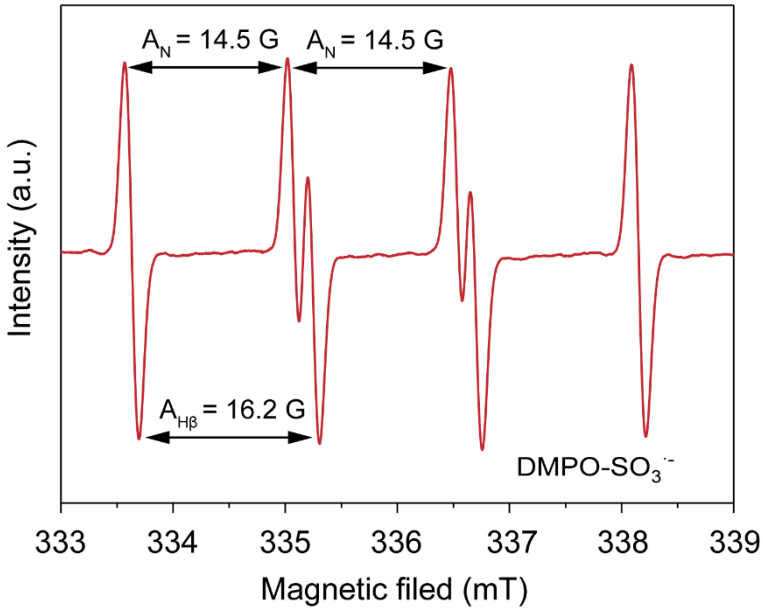

Fig. S3. DMPO spin-trapping EPR spectra of $SO_3^{\bullet-}$ in the H_2IrCl_6-$NaHSO_3$ systems.

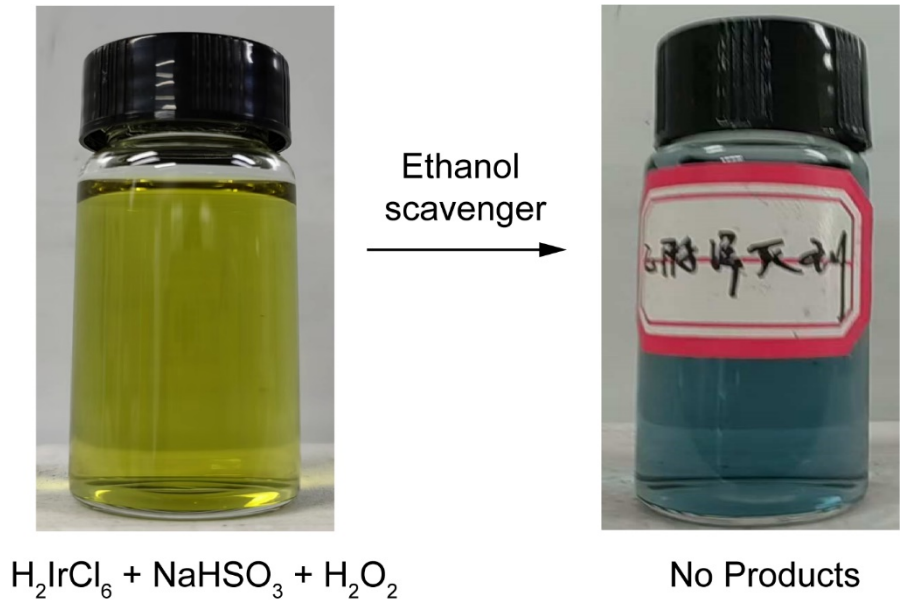

Fig. S4. The ethanol scavenger was introduced into the H_2IrCl_6-$NaHSO_3$-H_2O_2 systems.

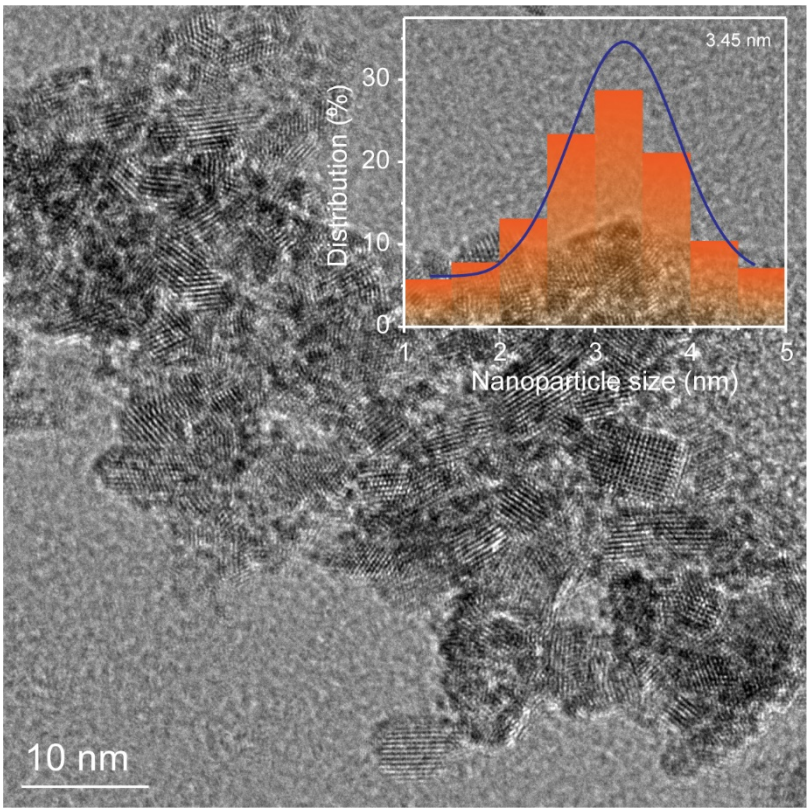

Fig. S5. HRTEM images of IrO_2 (Com.). Inset is the particle size analysis of the IrO_2 (Com.).

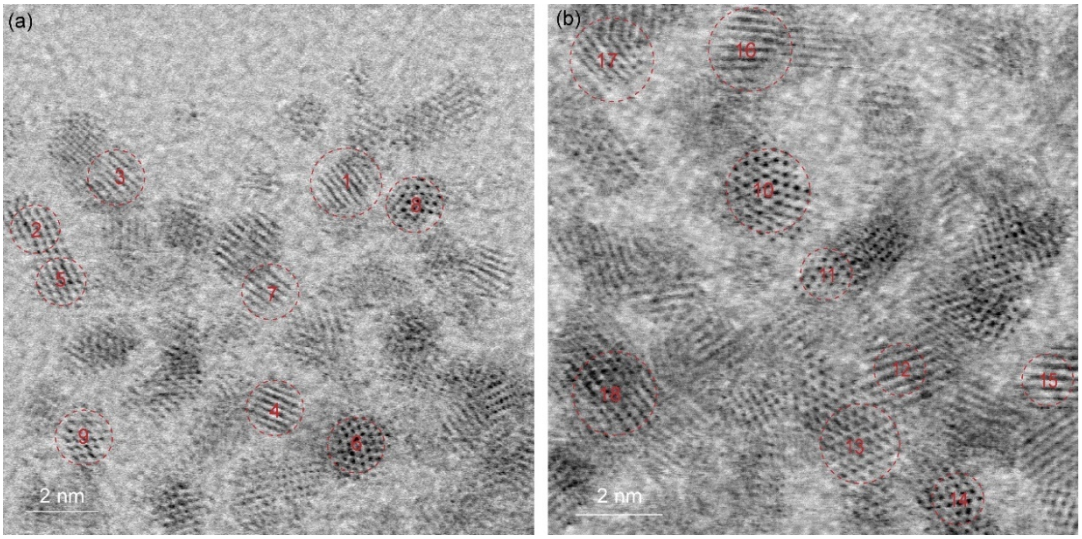

Fig. S6. ABF-STEM images of IrO_2 (Sub-2 nm) catalyst particles used for d-spacing measurements.

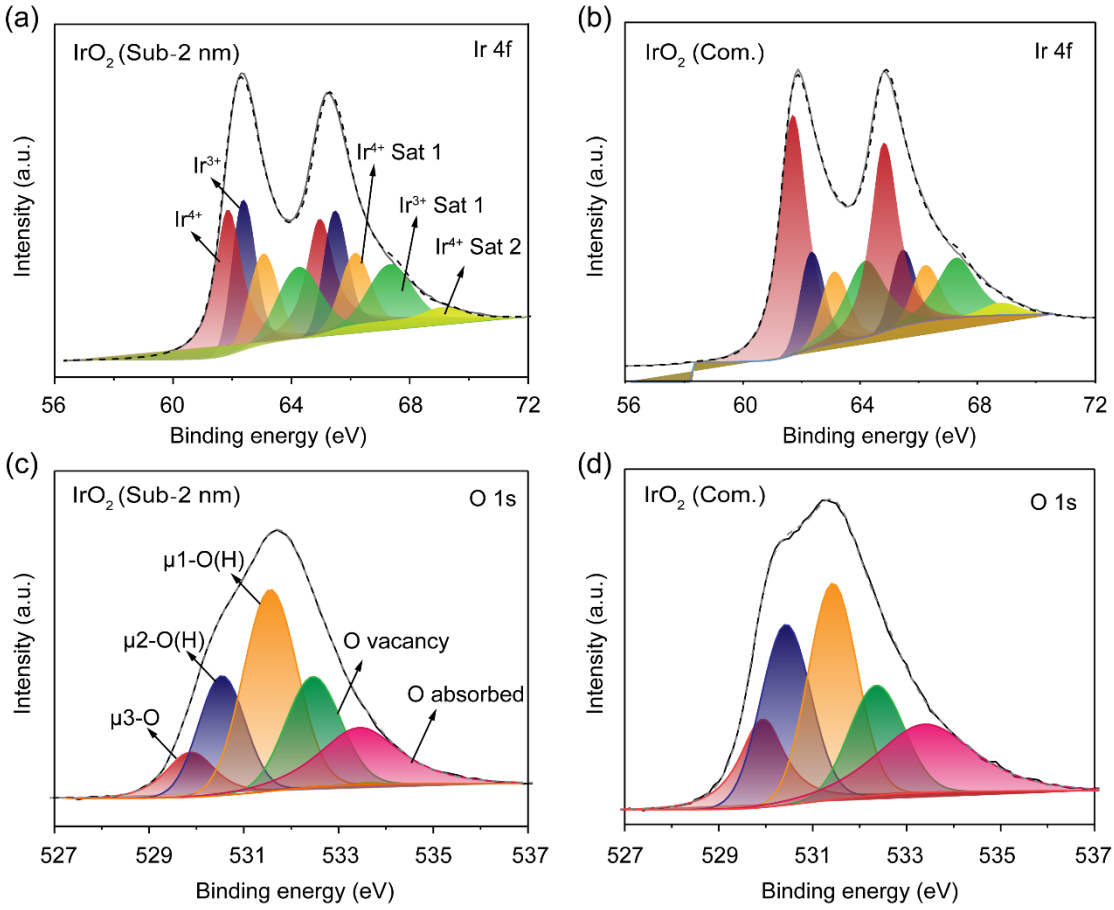

Fig. S7. Ir 4f XPS spectra of (a) IrO_2 (Sub-2 nm) and (b) IrO_2 (Com.) . O1s deconvoluted peaks of (c) IrO_2 (Sub-2 nm) and (d) IrO_2 (Com.).

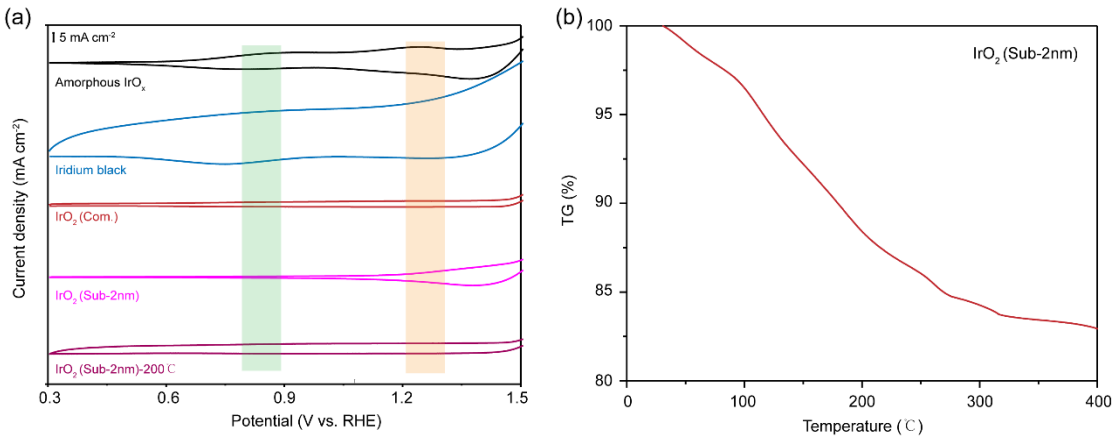

Fig. S8. (a) Cyclic voltammogram of the amorphous IrOx, iridium black, IrO_2(Com.), IrO_2 (Sub-2nm) and IrO_2 (Sub-2nm)-200℃. (b) TG curve of IrO_2 (Sub-2 nm) with a heating rate of 5°C/min under a nitrogen atmosphere.

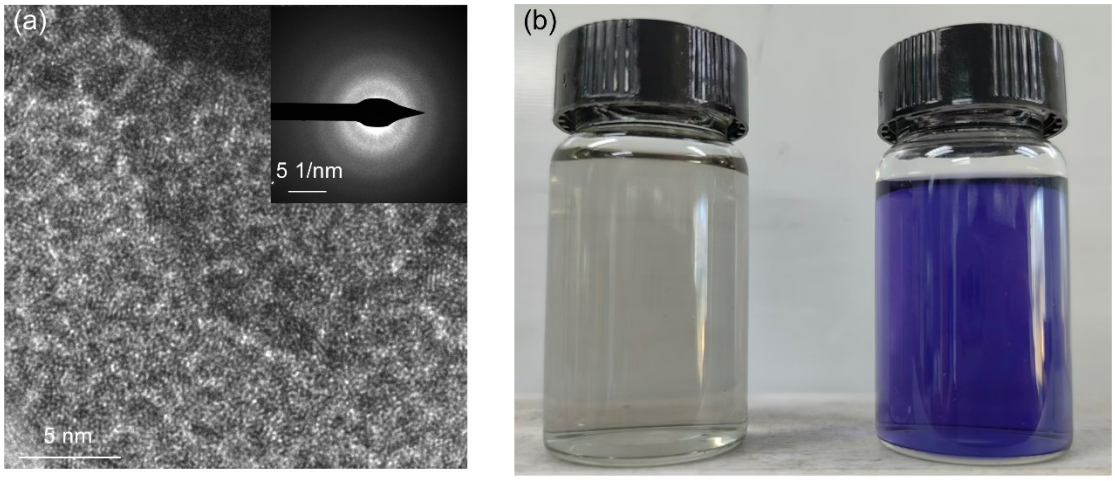

Fig. S9. Effect of pH on the synthesis in the H_2IrCl_6-$NaHSO_3$-H_2O_2 system. (a) HRTEM image of IrO_x synthesized at pH=7 (denoted as IrO_x-pH=7), with the SAED pattern provided in the inset. (b) Photographs of the reaction products taken during synthesis at pH 3 (left) and pH 9 (right).

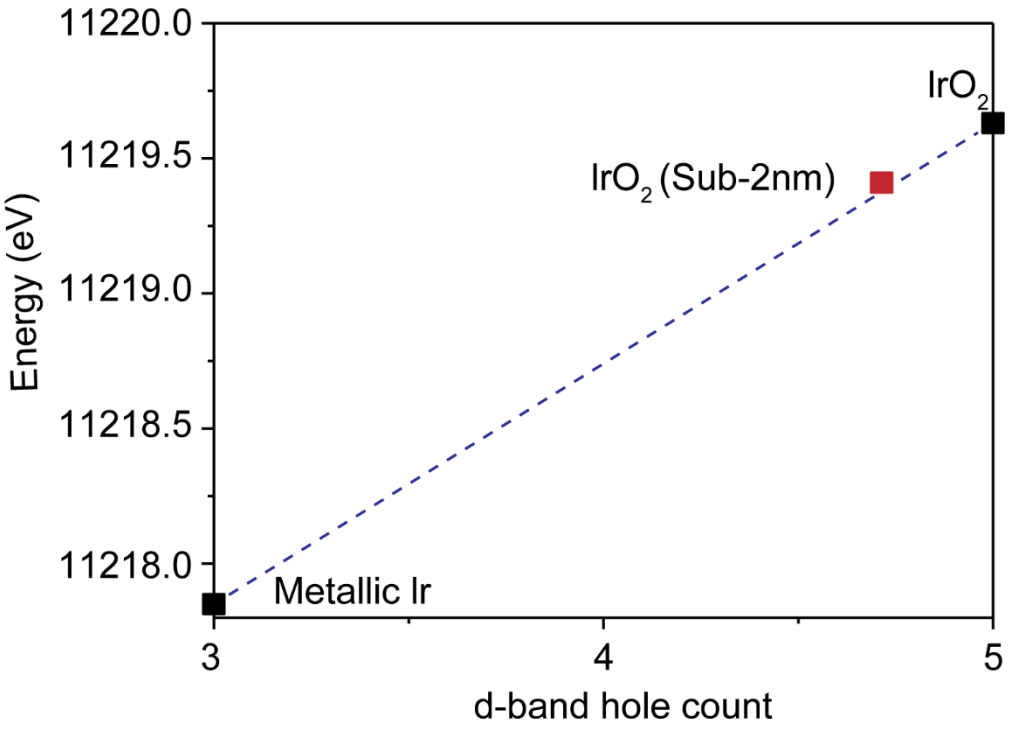

Fig. S10. Function between the position of white line peaks and d-band hole of IrO_2 (Sub-2 nm), IrO_2 and Ir foil.

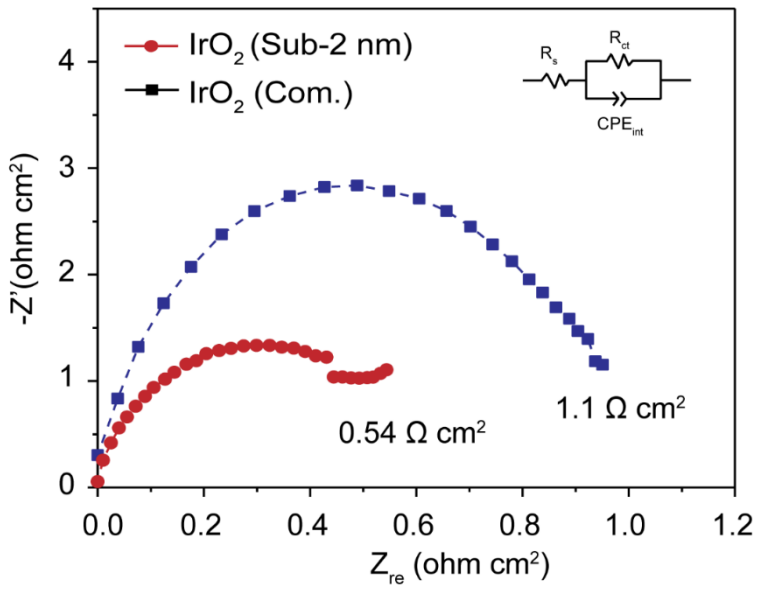

Fig. S11. Nyquist plots at 1.5 V vs RHE of IrO_2 (Sub-2 nm) and IrO_2 (Com.).

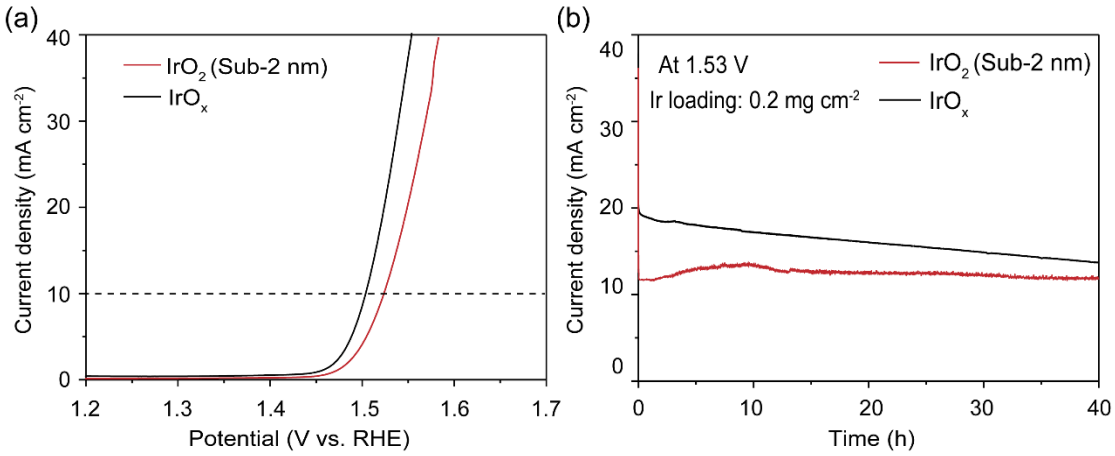

Fig. S12. (a) LSV curves and (b) Chronoamperometry stability tests of IrO_2 (Sub-2 nm) and IrO_x-pH=7.

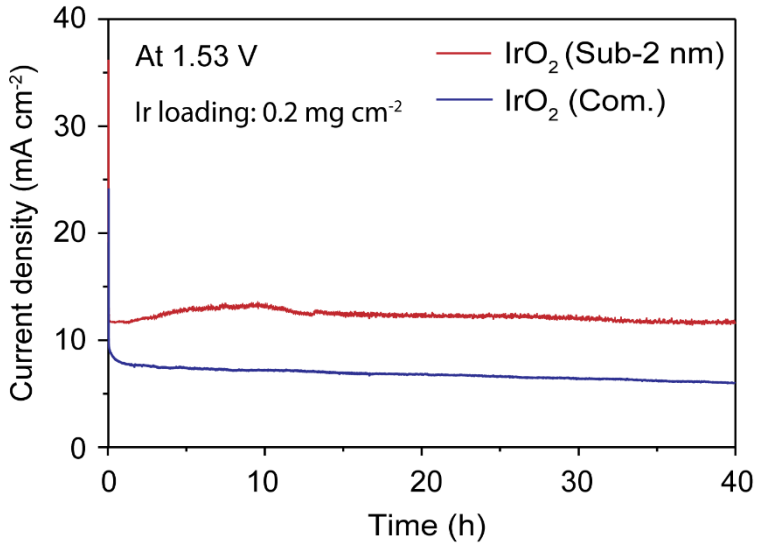

Fig. S13. Chronoamperometry stability tests of IrO_2 (Sub-2 nm) and IrO_2 (Com.) at 1.53 V vs. RHE for 40 h including online 100% iR-correction.

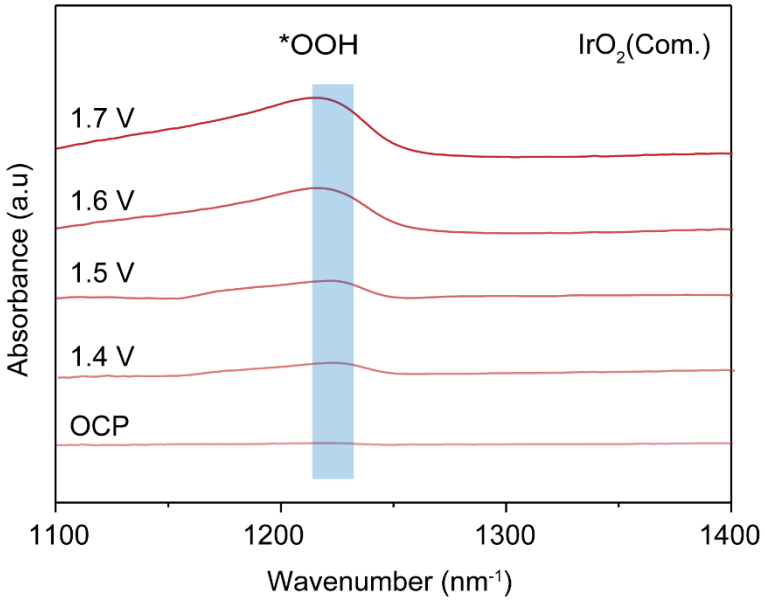

Fig. S14. In situ FTIR spectra of IrO_2 (Com.).

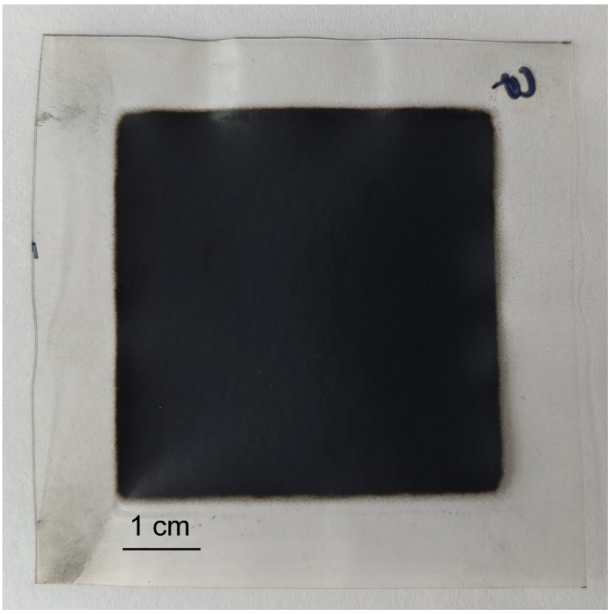

Fig. S15. The optical photo of the membrane electrode assembly.

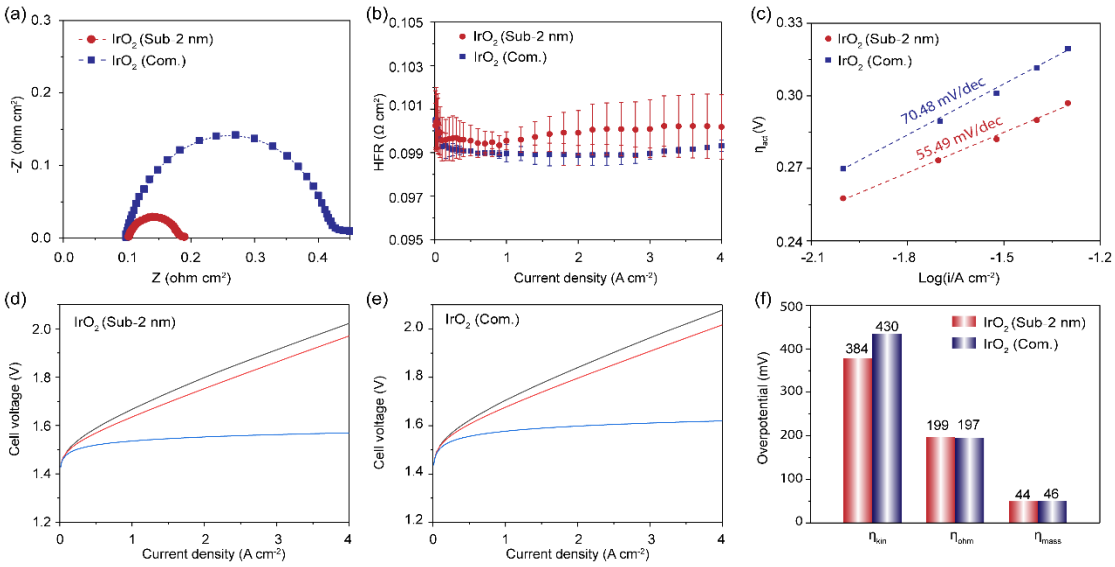

Fig. S16. (a) Nyquist plots at 1.5V, (b) HFR-values vs. current density obtained by electrochemical impedance spectroscopy. (c) Tafel slopes of IrO_2(Sub-2 nm) and IrO_2 (Com.). (d) Breakdown of ohmic overpotential (η_{ohm}), kinetic overpotential (η_{kin}), and transport overpotential (η_{trans}) of PEMWE single cells using (d) IrO_2(Sub-2 nm) and (e) IrO_2 (Com.). (f) Comparison of η_{kin}, η_{ohm} and η_{mt} for IrO_2(Sub-2 nm) and IrO_2 (Com.) at 2A/cm^{-2}.

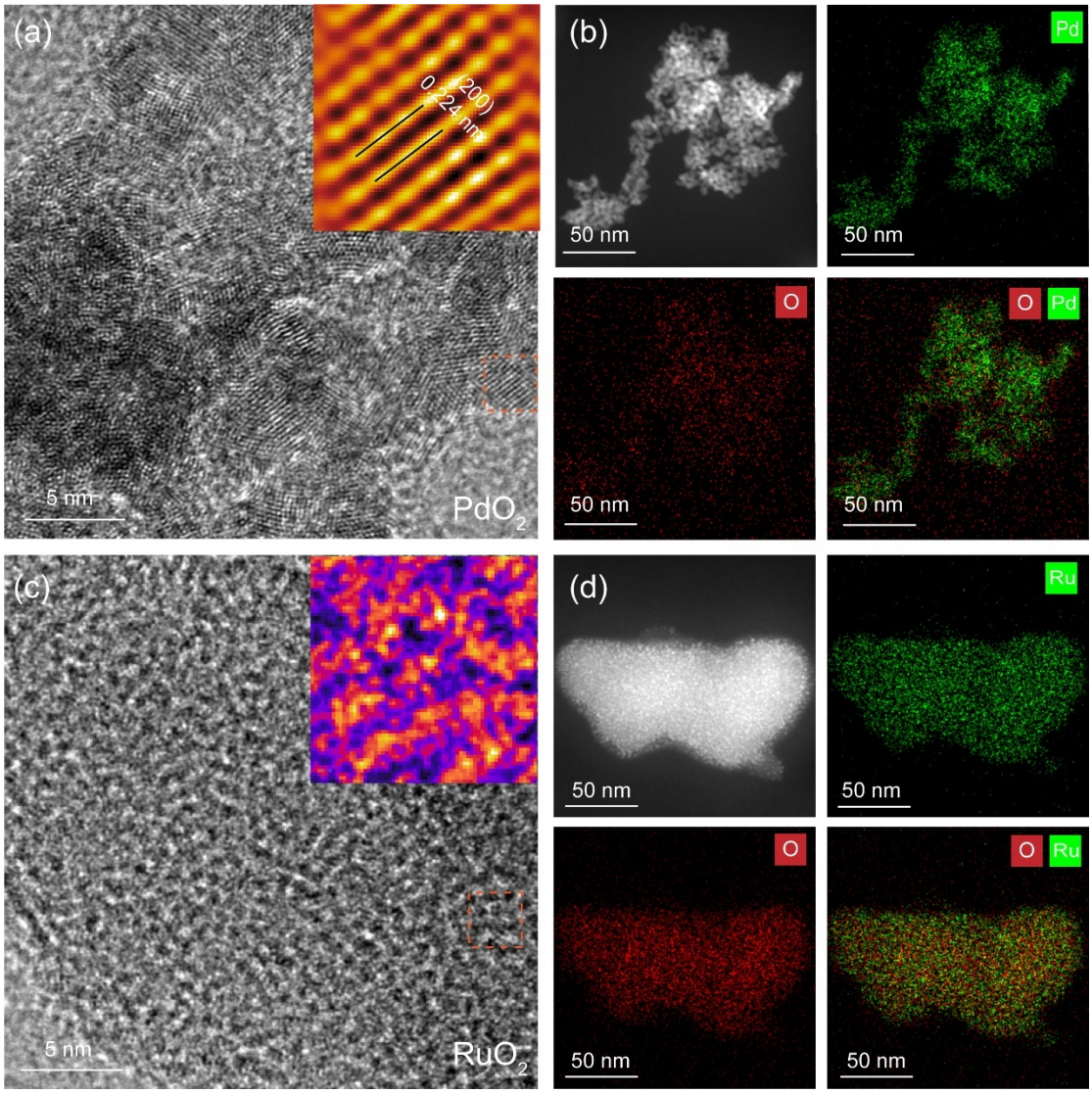

Fig. S17. (a) HRTEM images of PdO_2 by the same synthesis method. The inset shows IFFT images. (b) HAADF-STEM images and corresponding element mapping images: Pd, O and mix of PdO_2. (c) TEM images of RuO_2 by the same synthesis method. The inset shows IFFT images. (d) HAADF-STEM images and corresponding element mapping images: Ru, O, and mix of RuO_2.

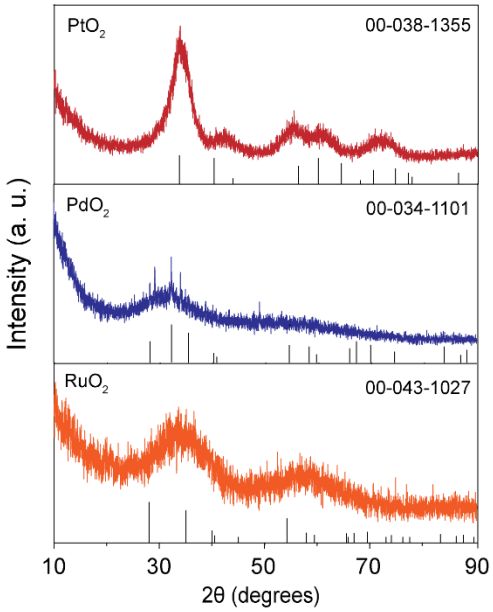

Fig. 18 Powder X-ray diffraction patterns of the PtO_2, PdO_2 and RuO_2

Table S1. Lattice spacings measured from TEM images of the IrO_2 (Sub-2nm) for 18 particles and their comparison to the closest matching IrO_2.

Particle	Measured d-spacing / Å	Closest *d*-spacing in tetragonal IrO_2/Å
1	2.17	2.25 (200)
2	2.37	2.25 (200)
3	2.38	2.25 (200)
4	2.10	2.01 (210)
5	2.26	2.25 (200)
6	2.48	2.58 (101)
7	2.42	2.58 (101)
8	2.10	2.01 (210)
9	2.31	2.25 (200)
10	2.30	2.25 (200)
11	2.25	2.25 (200)
12	2.49	2.58 (101)
13	2.20	2.25 (200)
14	2.31	2.25 (200)
15	2.68	2.58 (101)
16	2.37	2.25 (200)
17	2.08	2.01 (210)
18	2.48	2.58 (101)

Sample	Path	N[a]	R (Å)[b]	σ^2(Ø 10^{-3} Å^2)[c]	E_0(eV)[d]	R-factor
Ir foil	Ir-Ir	12	2.47+/-0.004	4.33+/-2.75	-0.57+/-0.67	0.009
IrO_2 (Sub-2nm)	Ir-O	5.54(0.61)	1.95 (0.01)	2.65(1.04)	7.14(1.93)	0.013
IrO_2	Ir-O	6	1.98 (0.01)	3.2	11.3(1.2)	0.0148

Table S2. EXAFS fitting parameters of Ir L_3 edge for various samples.

[a]*CN*, coordination number; [b]*R*, distance between absorber and backscatter atoms; [c]σ^2, Debye-Waller factor to account for both thermal and structural disorders; [d]ΔE_0, inner potential correction; *R* factor indicates the goodness of the fit. S_0^2 was fixed to 0.87, according to the experimental EXAFS fit of Ir foil by fixing CN as the known crystallographic value. A reasonable range of EXAFS fitting parameters: $0.600 < S_0^2 < 1.000$; $CN > 0$; $\sigma^2 > 0$ Å^2; $|\Delta E_0| < 15$ eV; *R* factor < 0.02.

Table S3. Comparison of the performance of IrO_2 (Sub-2nm) catalyst with other rutile IrO_2 catalysts reported in the literature.

NO.	Catalyst	Synthesis Method	Rutile IrO_2 Nanoparticle size	Mass-specific activity	Ref.
I	IrO_2 (Sub-2nm)	Free Radical Oxidation	1.6 nm	135 A/g @1.53V	This work
1	OMCD IrO_2/ATO	Organometallic chemical deposition	1-5 nm	73 A/g @1.525V	1
2	IrO_2PFHT	Perchlorate Fusion-Hydrothermal	2.1 nm	95A/g @1.525V	2
3	IrO_2 nanoneedles	Adams fusion	2.0 nm	61A/g @1.55V	3
4	Porous IrO_2	Adams fusion	1.7 nm	44A/g @1.525V	4
5	IrO_x-400℃	Sol-gel silica encapsulation	3.5 nm	700 A/g @1.525V	5

Table S4. Comparison between IrO_2 (Sub-2nm) and other reported catalysts in PEMWE.

NO.	Catalyst	Membrane Electrode Assembly			MEA performance		Stability	Reference
		Anode (mg_{Ir} cm^{-2})	Membrane	Cathode (mg_{Pt} cm^{-2})	Voltage at 2 A cm^{-2}, (V)	Activity (A cm^{-2}@1.9 V)		
I	IrO_2 (Sub-2nm)	0.3	N115	0.1	1.77	3.31	500 h@ 1 A cm^{-2}	This work
II	IrO_2(Com.)	0.3	N115	0.1	1.84	2.62	/	This work
1	Ir^{VI}-ado (MnO_2/p-PTL)	0.08	N115	0.2	1.77	3.1	2700 h@ 1.8 A cm^{-2}	6
2	IrO_2@TaB_2	0.15	N115	0.25	1.83	2.4	2 h@ 1 A cm^{-2}	7
3	Ir/B_4C	0.5	N115	0.4	1.8	2.6	50 h@ 1 A cm^{-2}	8
4	Ir/Nb_2O_{5-x}	3.0	N115	1.0	1.72	3.65	2000 h@ 2 A cm^{-2}	9
5	$Ir_{0.7}Ru_{0.3}O_2$	1.23	N115	0.5	1.850	/	48 h @1 A cm^{-2}	4
6	Ir/TiO_2-MoO_x	0.5	N115	0.5	1.872	/	50 h @1A cm^{-2}	10
7	Ir/ WO_xNRs-25	0.14	N115	0.4	1.95	1.7	1000 h @0.5Acm^{-2}	11
8	Ir/$W_xTi_{1-x}O_2$ (38 wt. %)	0.4	N115	0.4	1.76	/	1200 h @1.5Acm^{-2}	12
9	IrO_2/Ti (50 wt. %)	0.1	N115	0.25	2.1	1.5	1000 h @1 Acm^{-2}	13
10	p-L-IrO_2	0.56	N115	0.2	1.78	2.8	2000 h @1 A cm^{-2}	14
11	$Ir_{0.6}Sn_{0.4}O_2$	0.5	N115	0.4	1.963	1.75	100 h @1 A cm^{-2}	15
12	IrO_x-hybrid	0.2	N115	0.5	1.8	2.5	/	16
13	IrO_2 (SC)	0.4	N117	0.1	1.85	2.25	/	17
14	IrO_2 (TKK SA100)	0.17	N117	0.2	1.82	2.6	/	18
15	IrO_2@TiN_{1+x}	1.2	N117	0.4	1.916	1.8	100 h @1 A cm^{-2}	19
16	CrO_2-0.16IrO_2	0.59	N117	0.6	1.73	/	100 h @1 A cm^{-2}	20

17	$npIr_x$-NS	0.17	N117	/	1.85	2.4	/	21
18	IrO_2 (Nanoparticle)	2.0	N117	0.2	1.95	1.75	/	22
19	IrO_2 (Nanoparticle)	1.99	N117	1.19	1.9	2	/	23
20	IrRu HNWs	0.35	N212	0.4	1.81	2.5	240 h@ 2 A cm^{-2}	24
21	DNP-IrNi/Ti	0.67	N212	0.4	1.825	3.0	50 h @2 A cm^{-2}	25
22	Sr_2CaIrO_6	0.4	N212	0.4	1.81	3.15	450 h @2 A cm^{-2}	26
23	$IrO_2@TiO_2$	1.2	N212	0.5	1.717	4	/	27
24	Ir-NDs/ATO	1.0	N212	0.4	1.916	1.8	/	28
25	Ir-Ru (1:3)	0.158	N212	0.5	1.726	3.65	/	29
26	$W_{0.7}Ir_{0.3}O_y$	0.21	N212	0.2	/	0.6	/	30

Reference

1. Z. S. Rajan, T. Binninger, P. J. Kooyman, D. Susac and R. Mohamed, *Catalysis Science & Technology*, 2020, **10**, 3938-3948.
2. G. C. Moss, T. Binninger, Z. S. Rajan, B. J. Itota, P. J. Kooyman, D. Susac and R. Mohamed, *Small*, 2025, **21**, 2412237.
3. J. Lim, D. Park, S. S. Jeon, C. W. Roh, J. Choi, D. Yoon, M. Park, H. Jung and H. Lee, *Adv. Funct. Mater.*, 2018, **28**, 1704796.
4. M. Faustini, M. Giraud, D. Jones, J. Rozière, M. Dupont, T. R. Porter, S. Nowak, M. Bahri, O. Ersen and C. Sanchez, *Advanced Energy Materials*, 2019, **9**, 1802136.
5. M. Malinovic, P. Paciok, E. S. Koh, M. Geuß, J. Choi, P. Pfeifer, J. P. Hofmann, D. Göhl, M. Heggen and S. Cherevko, *Advanced Energy Materials*, 2023, **13**, 2301450.
6. A. Li, S. Kong, K. Adachi, H. Ooka, K. Fushimi, Q. Jiang, H. Ofuchi, S. Hamamoto, M. Oura and K. Higashi, *Science*, 2024, **384**, 666-670.
7. Y. Wang, M. Zhang, Z. Kang, L. Shi, Y. Shen, B. Tian, Y. Zou, H. Chen and X. Zou, *Nature communications*, 2023, **14**, 5119.
8. J. Islam, S.-K. Kim, P. T. Thien, M.-J. Kim, H.-S. Cho, W.-C. Cho, C.-H. Kim, C. Lee and J. H. Lee, *J. Power Sources*, 2021, **512**, 230506.
9. Z. Shi, J. Li, J. Jiang, Y. Wang, X. Wang, Y. Li, L. Yang, Y. Chu, J. Bai and J. Yang, *Angew. Chem. Int. Ed.*, 2022, **61**, e202212341.
10. E.-J. Kim, J. Shin, J. Bak, S. J. Lee, K. hyun Kim, D. Song, J. Roh, Y. Lee, H. Kim and K.-S. Lee, *Applied Catalysis B: Environmental*, 2021, **280**, 119433.
11. G. Jiang, H. Yu, Y. Li, D. Yao, J. Chi, S. Sun and Z. Shao, *ACS Applied Materials & Interfaces*, 2021, **13**, 15073-15082.
12. S. Zhao, A. Stocks, B. Rasimick, K. More and H. Xu, *J. Electrochem. Soc.*, 2018, **165**, F82.
13. C. Rozain, E. Mayousse, N. Guillet and P. Millet, *Applied Catalysis B: Environmental*, 2016, **182**, 123-131.
14. Z. Xie, X. Liang, Z. Kang, Y. Zou, X. Wang, Y. A. Wu, G. King, Q. Liu, Y. Huang and X. Zhao, *CCS Chemistry*, 2024, 1-13.
15. G. Jiang, H. Yu, J. Hao, J. Chi, Z. Fan, D. Yao, B. Qin and Z. Shao, *Journal of Energy Chemistry*, 2019, **39**, 23-28.
16. F. Hegge, F. Lombeck, E. Cruz Ortiz, L. Bohn, M. von Holst, M. Kroschel, J. Hübner, M. Breitwieser, P. Strasser and S. Vierrath, *ACS Applied Energy Materials*, 2020, **3**, 8276-8284.
17. S. M. Alia, S. Stariha and R. L. Borup, *J. Electrochem. Soc.*, 2019, **166**, F1164-F1172.
18. Z. Taie, X. Peng and D. Kulkarni, *ACS applied materials & interfaces, 12 (47)*, 2020.
19. G. Liu, J. Xu, Y. Wang and X. Wang, *Journal of Materials Chemistry A*, 2015, **3**, 20791-20800.

20. S. Ge, R. Xie, B. Huang, Z. Zhang, H. Liu, X. Kang, S. Hu, S. Li, Y. Luo and Q. Yu, *Energy & Environmental Science*, 2023, **16**, 3734-3742.
21. S. Chatterjee, X. Peng, S. Intikhab, G. Zeng, N. N. Kariuki, D. J. Myers, N. Danilovic and J. Snyder, *Advanced Energy Materials*, 2021, **11**, 2101438.
22. Y. Shi, Z. Lu, L. Guo and C. Yan, *Int. J. Hydrogen Energy*, 2017, **42**, 26183-26191.
23. F. Fouda-Onana, M. Chandesris, V. Médeau, S. Chelghoum, D. Thoby and N. Guillet, *Int. J. Hydrogen Energy*, 2016, **41**, 16627-16636.
24. L. Tao, F. Lv, D. Wang, H. Luo, F. Lin, H. Gong, H. Mi, S. Wang, Q. Zhang and L. Gu, *Joule*, 2024, **8**, 450-460.
25. K.-R. Yeo, K.-S. Lee, H. Kim, J. Lee and S.-K. Kim, *Energy & Environmental Science*, 2022, **15**, 3449-3461.
26. M. Retuerto, L. Pascual, J. Torrero, M. A. Salam, Á. Tolosana-Moranchel, D. Gianolio, P. Ferrer, P. Kayser, V. Wilke and S. Stiber, *Nature Communications*, 2022, **13**, 7935.
27. C. Van Pham, M. Bühler, J. Knöppel, M. Bierling, D. Seeberger, D. Escalera-López, K. J. Mayrhofer, S. Cherevko and S. Thiele, *Applied Catalysis B: Environmental*, 2020, **269**, 118762.
28. H.-S. Oh, H. N. Nong, T. Reier, M. Gliech and P. Strasser, *Chemical Science*, 2015, **6**, 3321-3328.
29. T. Hrbek, P. Kúš, Y. Kosto, M. G. Rodríguez and I. Matolínová, *J. Power Sources*, 2023, **556**, 232375.
30. T. Yan, S. Chen, W. Sun, Y. Liu, L. Pan, C. Shi, X. Zhang, Z.-F. Huang and J.-J. Zou, *ACS Applied Materials & Interfaces*, 2023, **15**, 6912-6922.